

Classifier-guided registration of coronary CT angiography and intravascular ultrasound

Rudolf L.M. van Herten, José P. Henriques, R. Nils Planken, Joost Daemen, Eline M.J. Hartman, Jolanda J. Wentzel, Ivana Išgum

Abstract—Coronary CT angiography (CCTA) and intravascular ultrasound (IVUS) provide complementary information for coronary artery disease assessment, making their registration valuable for comprehensive analysis. However, existing registration methods require manual interaction or extensive segmentations, limiting their practical application. In this work, we present a fully automatic framework for CCTA-IVUS registration using deep learning-based feature detection and a differentiable image registration module. Our approach leverages a convolutional neural network trained to identify key anatomical features from polar-transformed multiplanar reformatted CCTA or IVUS data. These detected anatomical features subsequently guide a differentiable registration module to optimize transformation parameters of an automatically extracted coronary artery centerline. The method does not require landmark selection or segmentations as input, while accounting for the presence of IVUS guidewire artifacts. Evaluated on 48 clinical cases with reference CCTA centerlines corresponding to IVUS pullback, our method achieved successful registration in 83.3% of cases, with a median centerline overlap F_1 -score of 0.982 and median cosine similarities of 0.940 and 0.944 for cross-sectional plane orientation. Our results demonstrate that automatically detected anatomical features can be leveraged for accurate registration. The fully automatic nature of the approach represents a significant step toward streamlined multimodal coronary analysis, potentially facilitating large-scale studies of coronary plaque characteristics across modalities.

Index Terms—Convolutional neural networks, coronary CT angiography, intravascular ultrasound, anatomical feature detection, multimodality image registration

I. INTRODUCTION

CORONARY artery disease (CAD) remains a leading cause of morbidity and mortality worldwide, necessitating tools for accurate and efficient diagnosis [1]. An established technique for the non-invasive identification and exclusion of patients with suspected CAD is coronary CT angiography (CCTA) [2], [3]. CCTA offers a comprehensive visualization of coronary anatomy, thus allowing experts to grade the severity of present stenosis and to quantify the extent and composition of plaque burden [4]. Despite its wide use in clinical practice, the spatial resolution of CCTA remains limited for a detailed analysis of plaque morphology and composition compared to intravascular imaging modalities. This constraint hampers accurate assessment of vulnerable lipid-rich plaques and subtle vessel wall changes, potentially affecting the prediction of adverse cardiovascular events [5].

To address the limitations of non-invasive imaging, invasive coronary imaging techniques such as intravascular ultrasound (IVUS) may be employed. These techniques are considered the reference standard for evaluating plaque pathology, offering superior spatial resolution and high-fidelity visualizations of coronary arteries [6]. This enables precise lumen measurements, detailed vessel wall analysis, and accurate characterization of atherosclerotic plaques [7].

While CCTA allows for an understanding of the 3D arterial geometry, IVUS provides a high-resolution visualization of arterial segments that allows for a detailed assessment of arterial wall morphology. As such, CCTA and IVUS are complementary imaging techniques. Hence, their registration offers a unique opportunity to conduct comprehensive coronary artery analyses. Many studies focusing on a combined analysis of CCTA and IVUS therefore rely on image registration [5], [8]–[10], which has been extensively explored. These works require an initial extraction of the coronary artery centerline, which is subsequently used to generate a stack of multiplanar reformatted (MPR) images from the CCTA that corresponds to the artery acquired during IVUS pullback (see Fig. 1). For example, Marquering *et al.* [11] proposed a multi-step approach to guide the image registration process, utilizing a combination of manually defined landmarks and automatic contour detection to interactively align the MPR volume and

Manuscript received Month XX, XXXX; accepted Month XX, XXXX. This study was funded by a private-public partnership grant provided by Health Holland, with contributions from B. Braun Melsungen AG, Melsungen, Germany, and Infraredx, Inc., Bedford, MA, USA (DEBuTLRP TKI-PPP, grant no. NCT04765956).

R.L.M. van Herten and I. Išgum are with the Department of Biomedical Engineering and Physics, Amsterdam Cardiovascular Sciences, Amsterdam UMC, 1105 AZ Amsterdam, The Netherlands, and also with the Informatics Institute, University of Amsterdam, 1090 GH Amsterdam, The Netherlands (e-mail: r.l.m.vanherten@amsterdamumc.nl; i.isgum@amsterdamumc.nl).

J.P. Henriques is with the Heart Centre, Academic Medical Centre, Amsterdam Cardiovascular Sciences, Heart failure & arrhythmias, 1105 AZ Amsterdam, The Netherlands (e-mail: j.p.henriques@amsterdamumc.nl).

R.N. Planken and I. Išgum are with the Department of Radiology and Nuclear Medicine, Amsterdam UMC, 1105 AZ Amsterdam, The Netherlands. R.N. Planken is also with the Department of Radiology, Mayo Clinic, 200 1st St SW, Rochester, MN 55905, United States (e-mail: r.n.planken@amsterdamumc.nl).

J. Daemen, E.M.J. Hartman, and J.J. Wentzel are with the Department of Cardiology, Erasmus MC, University Medical Center Rotterdam, 3015 GD Rotterdam, The Netherlands (e-mail: j.daemen@erasmusmc.nl; e.hartman@erasmusmc.nl; j.wentzel@erasmusmc.nl).

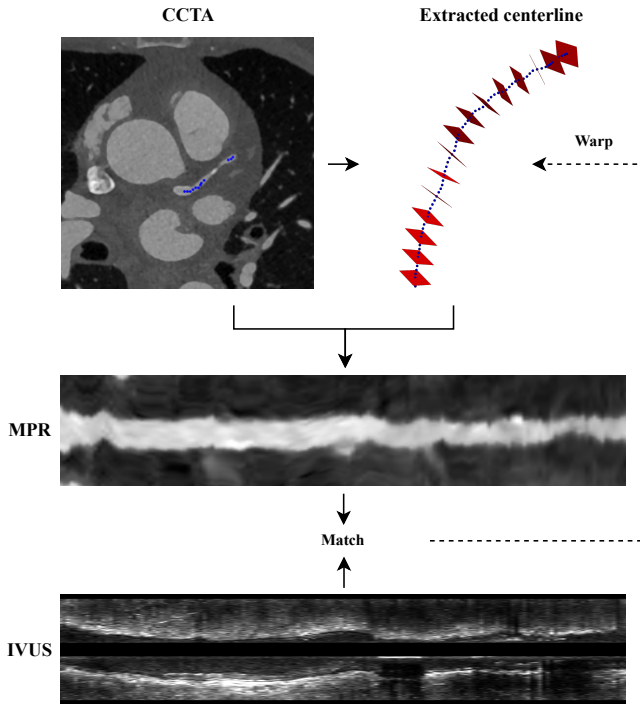


Fig. 1. A standard pipeline for CCTA-IVUS registration. An initial centerline extraction step allows for the identification of planes orthogonal to the centerline direction, producing a multi-planar reformation (MPR) of the CCTA coronary artery. The centerline is subsequently warped to match the IVUS based on some matching criterion between the MPR and the IVUS, typically guided by manually defined landmarks or image segmentations.

the IVUS image. Similarly, Van der Giessen *et al.* [12] proposed the utilization of user-defined landmarks to establish global bifurcation correspondences. Matched CCTA-derived MPR images are subsequently manually rotated to match the orientation of the IVUS pullback, after which the CCTA centerline is linearly interpolated between bifurcation correspondences to generate the full MPR image stack. Alternatively, methods have been proposed that require a combination of global manual alignment or seed point selection as well as image segmentations to guide CCTA-IVUS registration [13], [14]. While these approaches have advanced multimodality image registration, it is worth noting that they often rely on semi-automatic processes and require varying degrees of user input or additional segmentations, which is time-consuming and challenging, and may hamper their efficiency in clinical or research contexts.

Despite the surge of deep learning-based image registration (DLIR) over the last decade, its application to CCTA-IVUS registration has received little attention. This can be attributed to several factors. First, the registration problem is fundamentally different from affine or deformable image registration, where the input image volumes share a similar 3D coordinate system and feature mostly the same context window. Such methods process image pairs with deep neural networks to directly predict either an affine transformation matrix or a deformation vector field [15]–[17]. In contrast, for CCTA-IVUS registration, a minimal subset of the CCTA

image information corresponds to the IVUS pullback data, necessitating a more explicit method for the identification and matching of anatomical features. Second, intensity-based similarity metrics are ill-defined for the registration of non-invasive CCTA and invasive IVUS, which are a critical component for the optimization of most DLIR pipelines. Ultrasound imaging in particular has seen limited success in intensity-based multimodal registration. While normalized mutual information (NMI) and modality-independent neighborhood descriptors have shown promise in cross-modality registration tasks [18]–[20], their effectiveness for CCTA-IVUS registration is compromised by the presence of acoustic shadow artifacts in IVUS images. Alternatively, automatically extracted landmarks may be leveraged to guide DLIR, as demonstrated by Wang *et al.* [21]. However, this method assumes the presence of globally identifiable landmarks that remain consistent across all input image pairs. This assumption does not hold for coronary arteries, for which the locations of bifurcations and stenoses vary significantly between patients and different segments of the same artery.

In this paper, we introduce a fully automatic pipeline for CCTA-IVUS registration that addresses these challenges. Our approach consists of two main components. First, we propose a weakly-supervised method for deep learning-based key anatomical feature detection from CCTA-derived MPR or IVUS data. Similar to how classifier attention guides the image synthesis process in diffusion models [22], these classifier outputs are used to guide the registration pipeline, eliminating the need for manual landmark identification or extensive segmentations. Second, we propose a flexible and fully differentiable centerline deformation module, which dynamically updates the CCTA coronary artery centerline to align with the IVUS pullback data. The combined result is an automatic registration method for CCTA and IVUS alignment that operates without the need for segmentations or manual landmark selection as registration input. This has the potential to streamline subsequent analyses and enhance the clinical workflow for coronary artery assessment.

The remainder of this manuscript is structured as follows: Section II describes the dataset. Section III describes the methodology, for which experimental details are covered in Section IV. Results are presented in Section V, and are discussed in Section VI.

II. DATA

A. Patient and image data

This study comprises 48 patients retrospectively collected from the IMPACT study, a serial multimodality imaging study performed at the Erasmus University Medical Centre [23]. The median age was 68 years (range 44–76) years, and 42 patients were male.

Each patient underwent near-infrared spectroscopy (NIRS)-IVUS imaging (TVC Insight Coronary Imaging Catheter, InfraRedX, Burlington, MA, USA) of a non-treated vessel after successful percutaneous coronary intervention. Catheters were positioned distally from the distal sidebranch, upon which an automated pullback was performed. Pullback speed

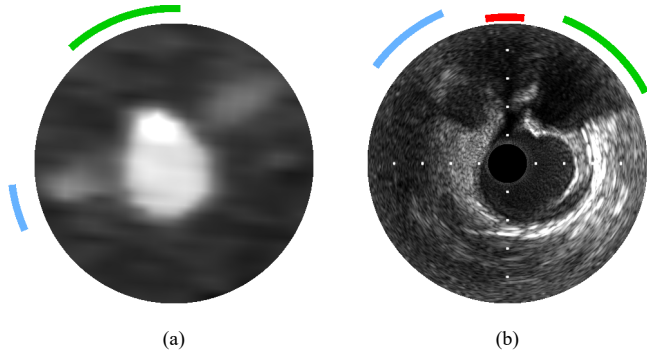


Fig. 2. Corresponding frames of a coronary artery in (a) a CCTA-derived MPR reconstruction, and (b) an IVUS pullback. Bifurcations (blue) and calcifications (green) are visible in both modalities and can be leveraged for alignment, while guidewire artifacts (red) may hamper registration due to a lack of correspondence between the MPR and IVUS image.

was 0.5 mm/s at 16 fps, with an in-frame resolution of 23 μm . IVUS images were retrospectively gated by selecting all frames that were located 6 frames before the R-peak.

CCTA exams were acquired at 1-month follow-up according to a standard prospective electrocardiogram-triggered clinical protocol (Somatom Force CT scanner, Siemens Healthineers, Erlangen, Germany). The median tube voltage was 80 kVp (range 70–120 kVp) and the median tube current was 1493 mAs (range 981–1952 mAs). Images were reconstructed to a median in-plane isotropic voxel size of 0.35 mm (range 0.29–0.44 mm) with a slice thickness and increment of 0.5 mm.

B. Reference standard

For all gated IVUS pullbacks, corresponding coronary artery centerlines and resulting MPRs were identified in the CCTA exams by matching the large side branches visible in both modalities. Throughout the remainder of this manuscript, we will refer to these CCTA-derived MPRs as MPRs for simplicity. For both MPR and IVUS data, bifurcations and calcifications were annotated along the angular (θ) and longitudinal (z) dimensions of the artery by transforming the data into a cylindrical coordinate system. Presence of calcifications in MPR data was determined visually and was guided by the presence of calcifications in corresponding IVUS frames. This effectively results in a 2D (θ, z) reference for every 3D (r, θ, z) MPR or IVUS volume. For IVUS images, the presence of any guidewire artifacts was additionally annotated at 10-frame intervals. An example of reference annotations in corresponding MPR and IVUS frames is presented in Fig. 2.

III. METHOD

Here, we present a flexible framework for the automatic alignment of CCTA and IVUS images. Our method comprises two main components. First, a convolutional neural network (CNN) is trained to identify key anatomical features from polar-transformed MPR or IVUS data, while the network additionally learns to detect guidewire artifacts in IVUS images. Second, once optimized, the CNN is used to guide a differentiable image registration module which optimizes a set of transformation matrices that optimally aligns an IVUS and a corresponding automatically extracted coronary artery centerline in CCTA.

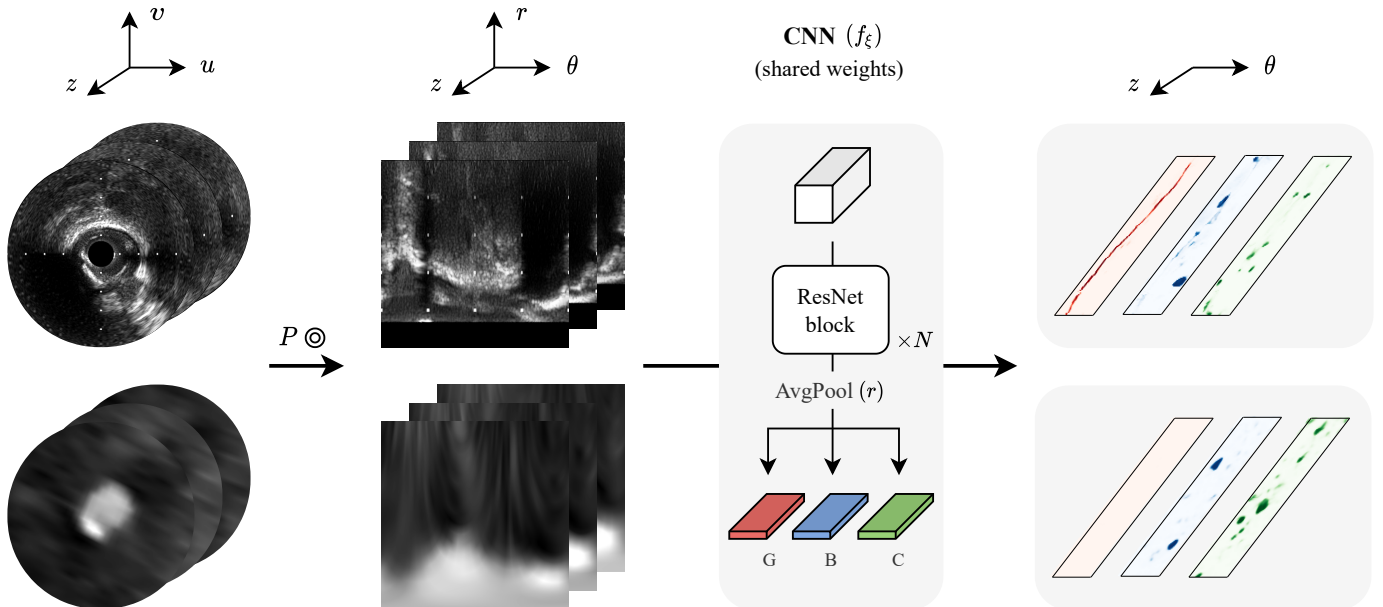


Fig. 3. Overview of key feature identification from MPR and IVUS image data. Images are first transformed from a locally Euclidian (u, v, z) to a cylindrical (r, θ, z) representation through a polar grid sampler P . A CNN is trained to accept both polar-transformed MPR and IVUS images, which are processed by a sequence of ResNet blocks and subsequently aggregated along the r -dimension to predict the presence of guidewire artifacts (G), bifurcations (B), and calcifications (C).

A. MPR and IVUS feature detection

For the alignment of different image modalities that represent the same anatomical structure, the identification of features that are consistently visible across both modalities is crucial. Additionally, the identification of features that are inconsistent across modalities is necessary, as they lower the reliability of intensity-based matching criteria.

To this end, bifurcations, calcifications and guidewire artifacts (specific to IVUS) may be used as landmarks for alignment. However, semantic segmentation of such structures is cumbersome, and may even be ill-posed. For instance, accurately delineating calcifications in IVUS data is inherently limited due to the presence of acoustic shadow artifacts, which obscure the true extent of calcified regions (see Fig. 2b). In contrast, identifying the *presence* of such structures is a well-defined task, which can be achieved by analyzing intensity profiles in a cylindrical coordinate system (r, θ, z) . For a given intensity profile $x_{\theta,z}$ at a specific angle (θ) and longitudinal position (z) , a label can be assigned to indicate the presence of one of the aforementioned landmarks. These radial intensity profiles are sampled at size 64 with a resolution of 0.07 mm and are spaced at 48 equiangular intervals. MPR volumes are further resampled to a through-plane resolution of 0.3 mm.

A 3D CNN $f_{\xi}(\cdot)$ with parameters ξ is trained to process the local neighborhood of such polar-transformed MPR or IVUS data. The convolutional encoder used in this work consists of 5 basic ResNet skip-connection blocks [24] and does not include pooling. An average pooling layer subsequently aggregates the hidden state along the radial (r) dimension, resulting in a 2D (θ, z) output. A final linear layer is then applied to predict the presence of bifurcations, calcifications, and guidewire artifacts at each (θ, z) location. An overview of the classifier is presented in Fig. 3.

B. CCTA-IVUS registration

To address the challenge of CCTA-IVUS registration, we approach the task as a coronary artery centerline warping problem. It therefore requires fitting a set of transformation parameters that describe how a CCTA centerline should be modified to align with the frames obtained during IVUS pullback.

1) *Centerline transformation matrices*: We propose that centerline warping can be effectively described by a combination of global and local components. Globally, the centerline must be correctly spaced and displaced along the length of the artery to correspond with the IVUS pullback distance. Locally, individual centerline points require displacement and tangent plane rotation to align with the spatial position and orientation of the IVUS probe within the artery for each frame.

A significant challenge is that a standard 3D affine transformation matrix is inadequate for accurately describing CCTA centerline warping. This limitation arises from the local variations in movement and rotation of the IVUS catheter during pullback, which cannot be captured by a single, global transformation. Rather, a unique affine matrix needs to be established for each centerline point that includes both global and local parameters:

$$\begin{bmatrix} u'_p \\ v'_p \\ z' \\ 1 \end{bmatrix} = \mathbf{T}_g \mathbf{T}_{l,p} \begin{bmatrix} u_p \\ v_p \\ z \\ 1 \end{bmatrix}. \quad (1)$$

Here, \mathbf{T}_g consists of a set of global transformation parameters, and $\mathbf{T}_{l,p}$ describes the unique transformation for each local reference framework (u_p, v_p) of a point p along the centerline. Scaling and translation along the centerline reference $(z$ -axis) encompasses the two global parameters, while in-frame rotation and displacement describe the local transformations:

$$\mathbf{T}_g = \begin{bmatrix} 1 & 0 & 0 & 0 \\ 0 & 1 & 0 & 0 \\ 0 & 0 & s_z & t_z \\ 0 & 0 & 0 & 1 \end{bmatrix}, \quad (2)$$

$$\mathbf{T}_{l,p} = \begin{bmatrix} \cos(\theta_p) & -\sin(\theta_p) & 0 & 0 \\ \sin(\theta_p) & \cos(\theta_p) & 0 & 0 \\ 0 & 0 & 1 & 0 \\ 0 & 0 & 0 & 1 \end{bmatrix} \begin{bmatrix} 1 & 0 & 0 & t_{u,p} \\ 0 & 1 & 0 & t_{v,p} \\ 0 & 0 & 1 & 0 \\ 0 & 0 & 0 & 1 \end{bmatrix}. \quad (3)$$

This formulation results in a set of parameters ϕ_T that describe the transformation of the CCTA centerline to align with the IVUS pullback. Specifically, we have three parameters per IVUS frame: one for rotation (θ_p) and two for displacement $(t_{u,p}$ and $t_{v,p})$ in the local reference frame. Additionally, we have two global parameters: s_z for scaling and t_z for translation along the z -axis. Solving for these parameters provides a complete mapping between the CCTA centerline and the IVUS frames.

2) *Registration module*: Identifying the full set of transformation parameters ϕ_T can be described by a pairwise optimization problem with the IVUS as the fixed image F , and a CCTA moving image M with corresponding centerline C . The objective is to align the coordinates \mathbf{x} of F and M in the same canonical space, i.e.

$$F(\mathbf{x}) = (M \circ \phi_T(C))(\mathbf{x}) = M_w(\mathbf{x}), \quad (4)$$

where M_w describes the warped moving image. In practice, this alignment is achieved by operating on polar-transformed versions of both images. Let P denote the polar transform operator. We can then express our optimization problem as a loss minimization:

$$\hat{\phi}_T = \underset{\phi_T}{\operatorname{argmin}} \mathcal{L}_{sim}(P(F), P(M_w)) + \alpha \mathcal{L}_{reg}(\phi_T), \quad (5)$$

where \mathcal{L}_{sim} minimizes the image dissimilarity between the polar-transformed fixed and moving images, and \mathcal{L}_{reg} regularizes the transformation ϕ_T with weighting factor α . Specifically, \mathcal{L}_{sim} is defined by a combined Dice and cross-entropy loss (\mathcal{L}_{DiceCE}) between CNN classifier f_{ξ} outputs of the polar-transformed images [22], as well as the masked NMI loss [15]:

$$\mathcal{L}_{sim} = \mathcal{L}_{DiceCE}(f_{\xi}(P(F))_{BC}, f_{\xi}(P(M_w))_{BC}) + \mathcal{L}_{NMI}(P(F)_G, P(M_w)_G). \quad (6)$$

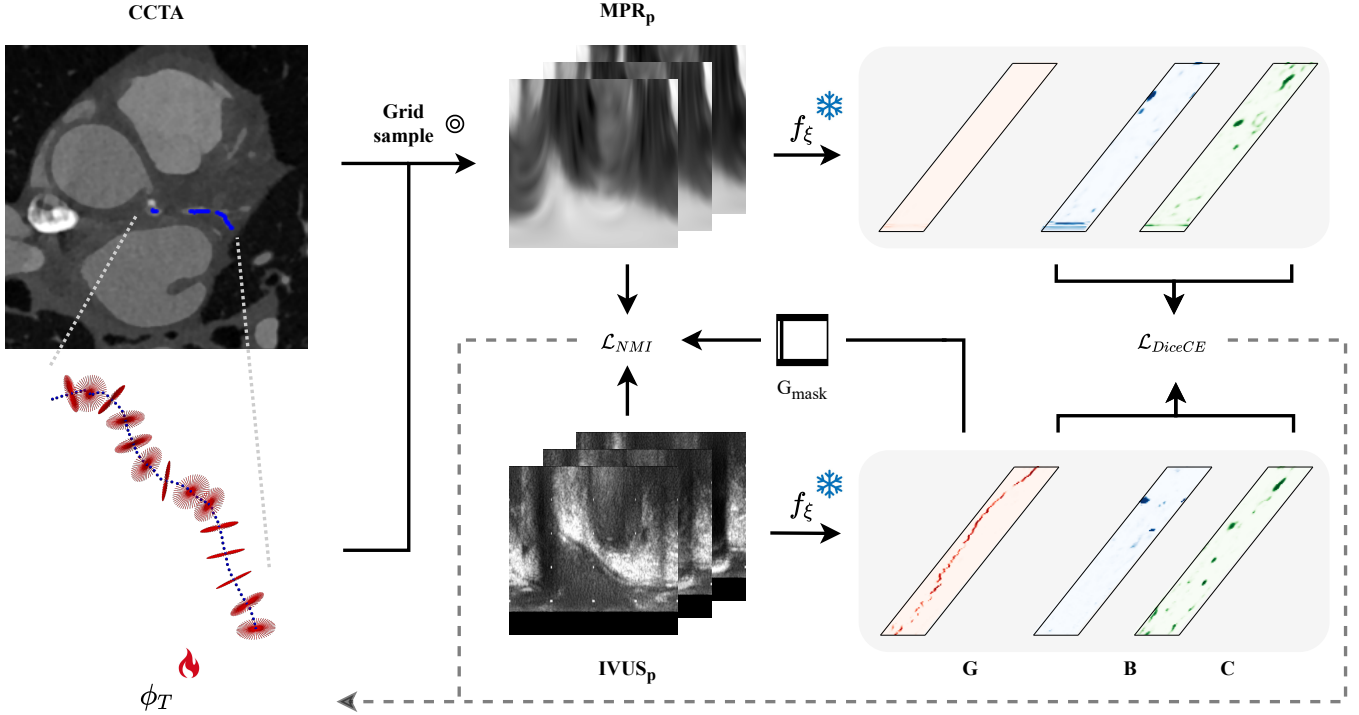


Fig. 4. Overview of the registration module. A CCTA moving image is sampled in polar coordinates along a coronary artery centerline, for which warping is defined by trainable transformation parameters ϕ_T . The frozen feature extraction CNN f_ξ processes the polar-transformed MPR and IVUS images to identify anatomical features and guidewire artifacts. The transformation parameters are optimized by evaluating the similarity between the warped moving image MPR_p and fixed image IVUS_p through an intensity-based loss \mathcal{L}_{NMI} and a Dice cross-entropy loss \mathcal{L}_{DiceCE} . \mathcal{L}_{NMI} is calculated for the masked image region where there is no guidewire interference, while \mathcal{L}_{DiceCE} reflects the correspondence of the detected anatomical features between image modalities.

In this loss formulation, f_ξ represents the CNN classifier which produces bifurcation (B) and calcification (C) probability outputs for both fixed and warped moving images. The subscript G denotes the binary guidewire mask obtained from $f_\xi(P(F))$ that excludes regions containing the IVUS guidewire from \mathcal{L}_{NMI} , as these regions lack meaningful correspondence between IVUS and CCTA images. Finally, \mathcal{L}_{reg} regularizes the delta between subsequent local transformation matrices $\mathbf{T}_{l,p}$:

$$\mathcal{L}_{reg} = \|\Delta(\theta_p + t_{u,p} + t_{v,p})\|_2^2. \quad (7)$$

An overview of the complete registration module is presented in Fig. 4.

3) *Global pre-alignment*: Given a differentiable moving image sampler, transformation parameters ϕ_T can be directly optimized using gradient descent methods. However, due to the presence of local minima in the optimal image alignment landscape, a coarse grid search is performed for parameter initialization. Initial alignment is exclusively guided by \mathcal{L}_{DiceCE} , and is conducted sequentially: first along the z -axis to establish approximate longitudinal alignment, followed by a search over rotation angles θ to determine the initial angular correspondence between IVUS and CCTA frames. Specifically, longitudinal correspondence is achieved by aggregating the 2D classifier output $f_\xi(P(\cdot))_{B,C}$ along the angular dimension using the maximum value:

$$\ell(z) = \max_{\theta} f_\xi(P(\cdot))_{B,C}(\theta, z), \quad (8)$$

where $\ell(z)$ represents the 1D signal used for initial z -axis alignment. Since the directionality of the extracted CCTA centerline cannot be guaranteed to be aligned with the IVUS pullback video, the global scaling parameter is initialized by evaluating both s_z and $-s_z$, where s_z is the ratio between the CCTA centerline length and IVUS pullback distance. After determining the optimal scaling direction, t_z is optimized through grid search to minimize \mathcal{L}_{DiceCE} between $\ell(z)$ signals of F and M_w . Subsequently, an initial uniform rotation θ_0 is determined for all points p by evaluating both clockwise (\mathbf{u}, \mathbf{v}) and anti-clockwise ($\mathbf{u}, -\mathbf{v}$) orientations of the plane-spanning vectors while minimizing \mathcal{L}_{DiceCE} over the full (θ, z) output space of f_ξ , such that $\theta_p = \theta_0$ for all p .

4) *Local optimization*: In this step, the full set of parameters ϕ_T is updated iteratively by minimizing both similarity and regularization losses through gradient descent. Starting from the global pre-alignment initialization, all parameters - including per-point local transformations $(\theta_p, t_{u,p}, t_{v,p})$ and global parameters (s_z, t_z) - are jointly optimized by minimizing eq. 5. This allows for fine-grained local adjustments while maintaining smooth transitions between adjacent frames through the regularization term \mathcal{L}_{reg} . The NMI component of the similarity loss \mathcal{L}_{NMI} is leveraged to achieve proper lumen alignment, and is calculated only in regions where the IVUS image is not corrupted by guidewire artifacts, as determined

by the binary mask G obtained from f_ξ (see Fig. 4).

IV. EXPERIMENTS

The 48 patients included in this study were divided into 5 folds for cross-validation to train and evaluate the classification algorithm. For subsequent registration experiments, these trained classification algorithms were used to guide the alignment process of the corresponding validation set. All experiments were performed on an NVIDIA GeForce RTX 2080 Ti GPU, and were implemented with the PyTorch deep learning library.

A. MPR and IVUS feature detection

Here, we detail the training methodology and evaluation for the classifier f_ξ .

1) *Experimental setup*: A single classifier was trained to process both MPR and IVUS data, with training samples randomly drawn from either modality to ensure balanced learning of both data types. Batches were further balanced to contain an equal ratio of bifurcations, calcifications, and regular coronary lumen. Samples were further augmented by randomly shifting the origin point of the polar transform by up to 0.6 mm, and by randomly flipping polar-transformed images along the θ and z -axis with $p = 0.5$.

The network, containing approximately 500K parameters, was optimized by minimizing both the Dice and binary cross-entropy loss for each class using AdamW [25] with a batch size of 32. Training consisted of two cosine annealing cycles of 40 and 80 epochs respectively, using an initial learning rate of $3e-4$ and a 40-epoch warmup period.

2) *Evaluation*: To evaluate classification performance, we computed both micro- and macro-averaged metrics for the detection of bifurcations, calcifications, and, in IVUS data, guidewire artifacts. Specifically, we calculated the precision, recall, and F_1 score for each object class. For micro-averaging, each (θ, z) prediction was treated individually, while for macro-averaging, metrics were first computed at the frame level (z) before averaging across the dataset.

TABLE I

CLASSIFICATION PERFORMANCE METRICS FOR DIFFERENT ANATOMICAL FEATURES IN BOTH IVUS AND MPR DATA. RESULTS ARE PRESENTED FOR BOTH MICRO- AND MACRO-AVERAGED METRICS ACROSS THE DATASET. FOR IVUS DATA, GUIDEWIRE ARTIFACTS (G), BIFURCATIONS (B), AND CALCIFICATIONS (C) WERE DETECTED, WHILE FOR MPR DATA ONLY BIFURCATIONS AND CALCIFICATIONS WERE CLASSIFIED.

		IVUS			MPR	
		G	B	C	B	C
Recall	Micro	0.821	0.525	0.777	0.584	0.649
	Macro	0.969	0.718	0.920	0.784	0.864
Precision	Micro	0.789	0.636	0.813	0.657	0.719
	Macro	1.000	0.660	0.733	0.693	0.700
F_1	Micro	0.805	0.575	0.794	0.618	0.682
	Macro	0.984	0.688	0.816	0.735	0.773

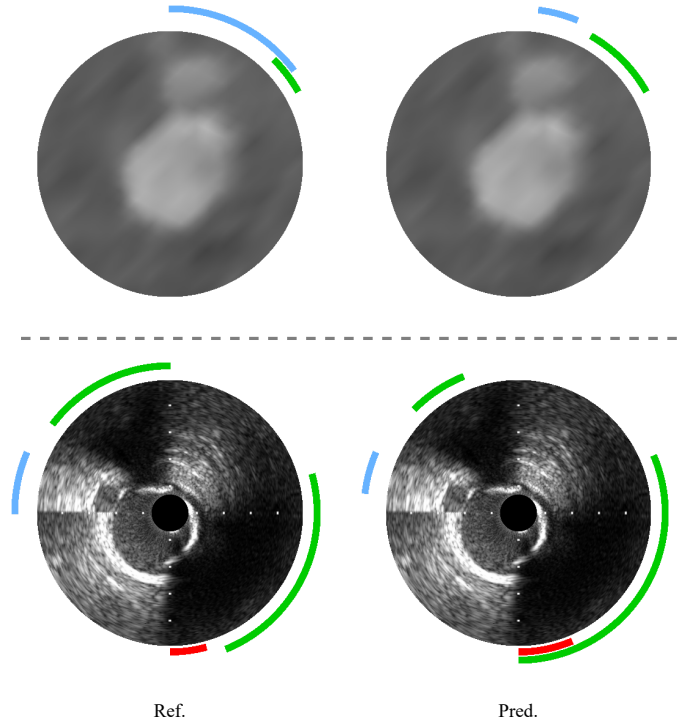


Fig. 5. Examples of classification performance. The top row shows MPR reference annotations (left) and corresponding predictions (right), while the bottom row presents IVUS data in the same format. In both modalities, blue regions denote bifurcations, green regions indicate calcifications, and for IVUS data, red annotations mark guidewire artifacts. While the predictions successfully identify all anatomical landmarks, discrepancies between reference and predictions arise from small differences in angular extent of the annotations, rather than missing or falsely detected structures.

B. CCTA-IVUS registration

Here, we describe the test-time registration optimization, along with details on the quantification of successful registration.

1) *Experimental setup*: Coronary artery centerlines were automatically extracted and labeled from CCTA scans using a previously developed automatic method [26]. For each vessel branch that underwent IVUS imaging, the corresponding CCTA centerline was extracted from its ostium to its distal terminus.

Centerline transformation parameters ϕ_T were optimized using AdamW with a constant learning rate of $1e-3$. Given the iterative nature of pairwise image registration, optimization continued until convergence, which was determined by monitoring the change in loss value between subsequent iterations. Specifically, optimization was terminated when the relative change in \mathcal{L}_{NMI} fell below a threshold of $1e-4$ for three consecutive iterations. The regularization weight α was set to 1000 to balance between image similarity and smooth local transformations.

2) *Evaluation*: Successful image registration was determined based on the overlap of the warped centerline with the reference, following the definition by Schaap *et al.* [27]. The warping performance was quantified using the harmonic mean of precision and recall (F_1 -score), where true positives (TP),

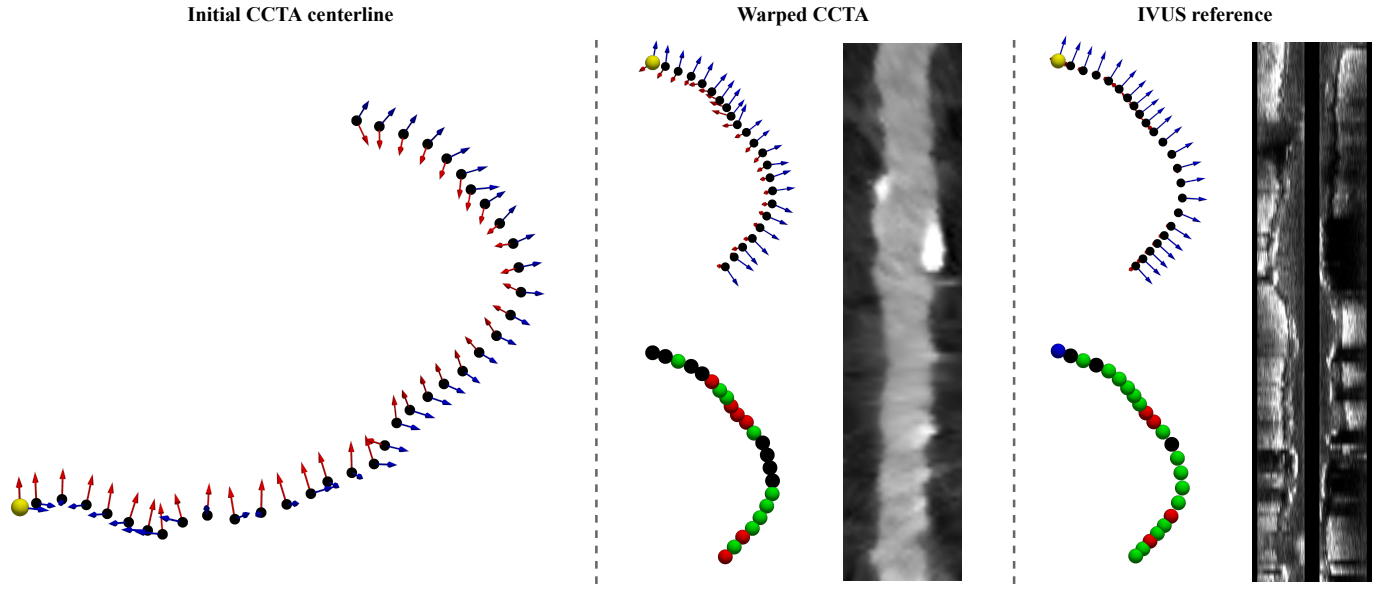


Fig. 6. Successful CCTA-IVUS registration of a right coronary artery (RCA). The left panel displays the automatically extracted RCA centerline from CCTA, with orthogonal planes defined by vectors u (red) and v (blue), and vessel direction indicated by the yellow starting point. The middle panel shows two views: the warped centerline with orthogonal plane directions (top) and the corresponding max-aggregated pointwise classification results (bottom). The right panel presents the IVUS reference data, including the centerline with orthogonal plane directions (top) and classification results (bottom). In the classification views, features are color-coded: blue for bifurcations, green for calcifications, and red for planes containing both. A longitudinal cross-section comparison of the warped CCTA MPR and IVUS demonstrates the achieved alignment. Centerlines are downsampled for improved interpretability.

false positives (FP), and false negatives (FN) were defined using a distance threshold of 2 mm, approximately equating the proximal radius of a coronary artery [28]. Additionally, we assessed the correctness of centerline MPR plane orientations by computing the cosine similarity between the predicted plane-spanning normal vectors (u , v) and their corresponding reference orientations. The cosine similarity ranges from -1 to 1, where 1 indicates perfect alignment, 0 indicates orthogonal vectors, and -1 indicates opposing directions.

V. RESULTS

We evaluate each step of the proposed registration pipeline separately to assess the performance of both the anatomical feature detection and the subsequent registration between CCTA and IVUS data.

A. Classification performance

The classification performance for anatomical features in both IVUS and MPR data is presented in Table I. For IVUS data, guidewire artifact detection achieved the highest performance with macro-averaged F_1 score of 0.977, followed by calcifications (0.781) and bifurcations (0.687). The detection of these features in MPR data showed similar trends, with calcifications and bifurcations achieving macro-averaged F_1 scores of 0.740 and 0.724, respectively. As expected for features that typically span multiple angular positions within a frame, macro-averaged metrics computed at the frame level consistently outperformed their micro-averaged counterparts that treated each angular prediction independently. Qualitative examples of the classification performance for both modalities are shown in Fig. 5.

B. Registration performance

The proposed registration method achieved high centerline overlap accuracy, with a median F_1 -score of 0.982 (IQR: 0.948-0.993). The orientation alignment of the cross-sectional MPR planes demonstrated strong agreement, with median cosine similarities of 0.940 (IQR: 0.870-0.975) and 0.944 (IQR: 0.881-0.978) for the first (u) and second (v) plane-spanning vectors, respectively.

Given an F_1 threshold of 0.8 and a cosine similarity of threshold of 0.75 to define successful registration, 40 out of 48 cases (83.3%) were successfully registered. Failure cases of the registration algorithm were attributed to two main factors: (1) IVUS scans containing none or only a single landmark (4 cases), resulting in multiple similar error minima during initial registration, and (2) poor CCTA image quality leading to incomplete or failed centerline extraction (4 cases). On average, registration took ~ 2 min. per image pair. A successful registration example is presented in Figure 6, while two failure cases are presented in Figure 7.

VI. DISCUSSION

In this work, we presented a fully automatic framework for CCTA-IVUS registration which, to the best of our knowledge, is the first of its kind. While several manual and semi-automatic approaches have been proposed, we eliminate user interaction through deep learning-based feature detection and differentiable image registration. Our method achieved successful registration in 83.3% of cases, with high centerline overlap accuracy (median F_1 -score: 0.982) and strong cross-sectional plane orientation agreement (median cosine similarities: 0.940 and 0.944 for respective plane-spanning vectors).

A key strength of our method lies in the flexibility of the registration module. While polar-transformed classifier outputs were chosen to guide the registration process, the architecture can be adapted to incorporate alternative guidance mechanisms, such as semantic segmentations or other feature detection methods. For example, implicit neural representations that directly map longitudinal positions to transformation parameters could enhance the current pairwise parameter optimization approach. Such networks have recently proven successful in other registration tasks [29].

Several practical assumptions were made in the development of this method. A constant heart rate during IVUS acquisition was assumed, leading to equidistant spacing of centerline points. While this simplification has proven effective in practice, inaccuracies might be introduced in cases with significant heart rate variability. Furthermore, out-of-plane rotations of the IVUS catheter were not accounted for, though this should affect results minimally since the catheter is physically constrained to remain near parallel to the vessel centerline direction during pullback. The results support this assumption, as high registration accuracy was achieved without explicitly modeling these rotations.

The classification performance revealed some notable differences between IVUS and MPR data. While separate classifiers for MPR and IVUS data were initially considered, a unified approach proved sufficient for registration purposes. The classifier occasionally confuses guidewire artifacts with calcifications in IVUS images, and calcifications generally appear more prominent in IVUS compared to CCTA. However, these discrepancies did not substantially impact the registration performance, suggesting that perfect classification is not required for successful alignment.

Given the differences in appearance between modalities, several matching criteria were explored. While Wasserstein distance could potentially be used to match bifurcations and calcifications between modalities, this metric is primarily designed for comparing probability distributions with equal total mass. Since the summed network predictions between IVUS and MPR data can differ, and the metric is sensitive to outliers, this matching approach proved less reliable. Instead, a combined Dice and cross-entropy loss was used to match these

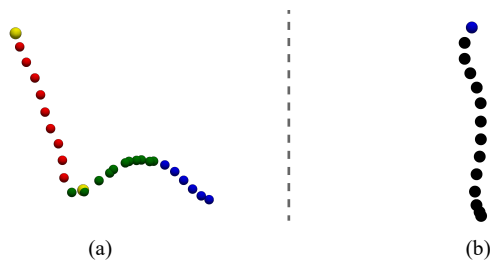


Fig. 7. Examples of registration failure modes. In (a), the limited initial overlap between the CCTA and IVUS centerlines causes global pre-alignment to fail. The image shows the IVUS centerline (blue), the automatically extracted centerline from CCTA (red), with overlap presented in green. (b) illustrates the pointwise aggregated classification result for an IVUS containing only a single bifurcation as a landmark (top), thus leading to multiple plausible options for CCTA-IVUS pre-alignment.

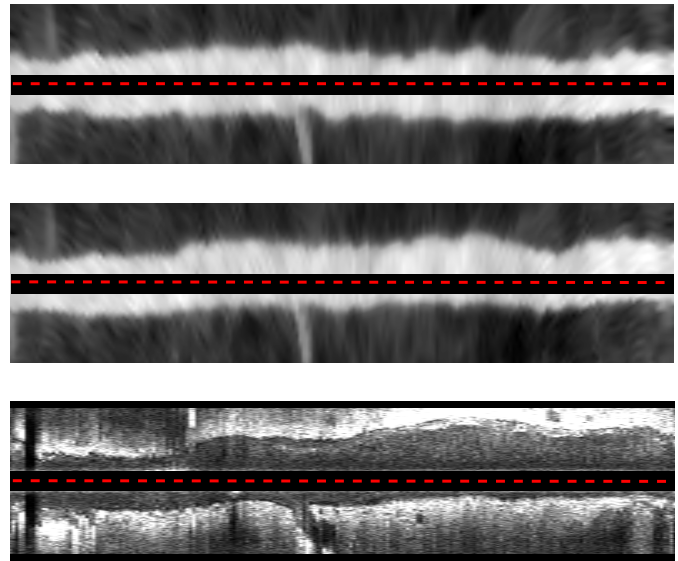


Fig. 8. Example illustrating the finetuning stage of the registration pipeline. Top: MPR reconstruction after initial global pre-alignment. Middle: The MPR reconstruction after subsequent gradient-descent-based image registration. Bottom: the corresponding IVUS pullback. The red dashed lines indicate the central image axis, which follows the path of the catheter for the IVUS image. Note how local optimization improves the alignment between the MPR and IVUS lumen boundaries.

anatomical features, while the NMI loss proved qualitatively effective for lumen matching (see Fig. 8). While direct evaluation of lumen alignment accuracy could prove beneficial, such validation is challenging due to inherent variations in lumen annotations between modalities and among different annotators.

An additional note should be made regarding the evaluation of the proposed method, as there is currently a lack of automatic reference standards for CCTA-IVUS registration. As existing approaches predominantly rely on manual interaction, direct performance comparisons are difficult to establish. While our results demonstrate good performance, the lack of automated approaches in this field makes comprehensive comparison with prior work challenging.

As the method relies on the identification of anatomical landmarks, registration accuracy correlates with their presence in the image data. IVUS pullbacks with multiple landmarks, particularly those with calcifications, typically demonstrated reliable registration outcomes. Notably, the method achieves high accuracy for highly diseased vessels, which are often cases of significant clinical interest. Nonetheless, two primary failure modes were identified: cases with very limited reference landmarks (particularly those with few bifurcations and no distinguishable plaque), where multiple similar error minima could lead to incorrect global alignment, and cases with poor CCTA image quality resulting in unreliable centerline extraction (see Fig. 7). The former limitation could potentially be addressed by incorporating additional matching criteria, such as including the prediction of the radial lumen extent in the polar domain for improved initial alignment. Such measures of lumen extent could provide valuable additional constraints for registration when minimal anatomical landmarks are present.

Several interesting directions could be explored in future work. First, the method should be validated on a larger clinical cohort to assess its performance across different vessels, patient populations, and scanner vendors for both CT and IVUS. Automatic registration could enable combined analysis of MPR and IVUS data, which would be particularly interesting when NIRS data is available. Such multi-modality analysis could potentially help to develop methods for direct lipid plaque detection from CCTA. These steps could contribute to better non-invasive plaque assessment from CCTA imaging.

In conclusion, we have demonstrated that fully automatic CCTA-IVUS registration is feasible and achieves robust performance. By eliminating the need for manual interaction while maintaining reliable performance, this work opens up possibilities for large-scale studies of coronary plaque characteristics and could potentially enhance clinical workflows for comprehensive coronary artery assessment.

REFERENCES

- [1] E. B. Komilovich, "Coronary artery disease," *European Journal of Modern Medicine and Practice*, vol. 3, no. 12, pp. 81–87, 2023.
- [2] P. Maurovich-Horvat *et al.*, "CT or invasive coronary angiography in stable chest pain," *New England Journal of Medicine*, vol. 386, no. 17, pp. 1591–1602, 2022.
- [3] C. D. Maroules *et al.*, "2022 use of coronary computed tomographic angiography for patients presenting with acute chest pain to the emergency department: An expert consensus document of the Society of cardiovascular computed tomography (SCCT): Endorsed by the American College of Radiology (ACR) and North American Society for cardiovascular Imaging (NASCI)," *Journal of Cardiovascular Computed Tomography*, vol. 17, no. 2, pp. 146–163, 2023.
- [4] R. C. Cury *et al.*, "CAD-RADS™ 2.0–2022 coronary artery disease-reporting and data system: an expert consensus document of the society of cardiovascular computed tomography (SCCT), the American college of cardiology (ACC), the American college of radiology (ACR), and the North America society of cardiovascular imaging (NASCI)," *Cardiovascular Imaging*, vol. 15, no. 11, pp. 1974–2001, 2022.
- [5] A. Ramasamy *et al.*, "Implications of computed tomography reconstruction algorithms on coronary atheroma quantification: comparison with intravascular ultrasound," *Journal of Cardiovascular Computed Tomography*, vol. 17, no. 1, pp. 43–51, 2023.
- [6] G. S. Mintz and G. Guagliumi, "Intravascular imaging in coronary artery disease," *The Lancet*, vol. 390, no. 10096, pp. 793–809, 2017.
- [7] T. J. Jun *et al.*, "Automated detection of vulnerable plaque in intravascular ultrasound images," *Medical & Biological Engineering & Computing*, vol. 57, pp. 863–876, 2019.
- [8] M. J. Boogers *et al.*, "Automated quantification of coronary plaque with computed tomography: comparison with intravascular ultrasound using a dedicated registration algorithm for fusion-based quantification," *European Heart Journal*, vol. 33, no. 8, pp. 1007–1016, 2012.
- [9] H. Matsumoto *et al.*, "Standardized volumetric plaque quantification and characterization from coronary CT angiography: a head-to-head comparison with invasive intravascular ultrasound," *European Radiology*, vol. 29, pp. 6129–6139, 2019.
- [10] E. Conte *et al.*, "Plaque quantification by coronary computed tomography angiography using intravascular ultrasound as a reference standard: a comparison between standard and last generation computed tomography scanners," *European Heart Journal-Cardiovascular Imaging*, vol. 21, no. 2, pp. 191–201, 2020.
- [11] H. A. Marquering *et al.*, "Coronary CT angiography: IVUS image fusion for quantitative plaque and stenosis analyses," in *Medical Imaging 2008: Visualization, Image-Guided Procedures, and Modeling*, vol. 6918. SPIE, 2008, pp. 499–508.
- [12] A. G. van der Giessen *et al.*, "3D fusion of intravascular ultrasound and coronary computed tomography for in-vivo wall shear stress analysis: a feasibility study," *The International Journal of Cardiovascular Imaging*, vol. 26, pp. 781–796, 2010.
- [13] Z. Qian, G. Vazquez, and S. Voros, "Intermodal registration of CTA and IVUS-VH, and its application on CTA-based plaque composition analysis," in *2011 IEEE International Symposium on Biomedical Imaging: From Nano to Macro*. IEEE, 2011, pp. 419–423.
- [14] L. Athanasiou *et al.*, "Three-dimensional reconstruction of coronary arteries and plaque morphology using CT angiography–comparison and registration with IVUS," *BMC Medical Imaging*, vol. 16, pp. 1–13, 2016.
- [15] B. D. de Vos, F. F. Berendsen, M. A. Viergever, H. Sokooti, M. Staring, and I. Išgum, "A deep learning framework for unsupervised affine and deformable image registration," *Medical Image Analysis*, vol. 52, pp. 128–143, 2019.
- [16] G. Balakrishnan, A. Zhao, M. R. Sabuncu, J. Guttag, and A. V. Dalca, "Voxelmorph: a learning framework for deformable medical image registration," *IEEE Transactions on Medical Imaging*, vol. 38, no. 8, pp. 1788–1800, 2019.
- [17] J. Chen, E. C. Frey, Y. He, W. P. Segars, Y. Li, and Y. Du, "Transmorph: Transformer for unsupervised medical image registration," *Medical Image Analysis*, vol. 82, p. 102615, 2022.
- [18] J. P. W. Pluim, J. A. Maintz, and M. A. Viergever, "Mutual-information-based registration of medical images: a survey," *IEEE Transactions on Medical Imaging*, vol. 22, no. 8, pp. 986–1004, 2003.
- [19] M. P. Heinrich *et al.*, "MIND: Modality independent neighbourhood descriptor for multi-modal deformable registration," *Medical Image Analysis*, vol. 16, no. 7, pp. 1423–1435, 2012.
- [20] I. Y. Ha and M. P. Heinrich, "Modality-agnostic self-supervised deep feature learning and fast instance optimisation for multimodal fusion in ultrasound-guided interventions," *Computer Methods and Programs in Biomedicine*, vol. 211, p. 106374, 2021.
- [21] A. Q. Wang, M. Y. Evan, A. V. Dalca, and M. R. Sabuncu, "A robust and interpretable deep learning framework for multi-modal registration via keypoints," *Medical Image Analysis*, vol. 90, p. 102962, 2023.
- [22] P. Dhariwal and A. Nichol, "Diffusion Models Beat GANs on Image Synthesis," *Advances in Neural Information Processing Systems*, vol. 34, pp. 8780–8794, 2021.
- [23] E. M. J. Hartman *et al.*, "Lipid-rich plaques detected by near-infrared spectroscopy are more frequently exposed to high shear stress," *Journal of Cardiovascular Translational Research*, vol. 14, pp. 416–425, 2021.
- [24] K. He, X. Zhang, S. Ren, and J. Sun, "Deep residual learning for image recognition," in *Proceedings of the IEEE Conference on Computer Vision and Pattern Recognition*, 2016, pp. 770–778.
- [25] I. Loshchilov *et al.*, "Fixing weight decay regularization in Adam," *arXiv preprint arXiv:1711.05101*, vol. 5, 2017.
- [26] N. Hampe *et al.*, "Graph neural networks for automatic extraction and labeling of the coronary artery tree in CT angiography," *Journal of Medical Imaging*, vol. 11, no. 3, pp. 034001–034001, 2024.
- [27] M. Schaap *et al.*, "Standardized evaluation methodology and reference database for evaluating coronary artery centerline extraction algorithms," *Medical Image Analysis*, vol. 13, no. 5, pp. 701–714, 2009.
- [28] J. T. Dodge Jr, B. G. Brown, E. L. Bolson, and H. T. Dodge, "Lumen diameter of normal human coronary arteries. Influence of age, sex, anatomic variation, and left ventricular hypertrophy or dilation," *Circulation*, vol. 86, no. 1, pp. 232–246, 1992.
- [29] J. M. Wolterink, J. C. Zwienenberg, and C. Brune, "Implicit neural representations for deformable image registration," in *International Conference on Medical Imaging with Deep Learning*. PMLR, 2022, pp. 1349–1359.